https://doi.org/10.5194/egusphere-2024-2026
Preprint. Discussion started: 7 August 2024

Contrasting patterns of change in snowline altitude across five Himalayan catchments

Orie Sasaki[1], Evan S. Miles[2], Francesca Pellicciotti[2], Akiko Sakai[1], Koji Fujita[1]

[1]Graduate School of Environmental Studies, Nagoya University, Nagoya, 484－8601, Japan
[2]Swiss Federal Institute for Forest, Snow, and Landscape Research WSL, Birmensdorf, CH-8903, Switzerland

Correspondence to: Orie Sasaki (Sasaki.o.ab@m.titech.ac.jp)

Abstract.

Seasonal snowmelt in the high mountains of Asia is an important source of river discharge. Therefore, observation of the spatiotemporal variations in snow cover at catchment scales using high-resolution satellites is essential for understanding changes in water supply from headwater catchments. In this study, we propose an algorithm to automatically detect the snowline altitude (SLA) using the Google Earth Engine platform with available high-resolution multispectral satellite archives that can be readily applied globally. Here, we applied and evaluated the tool to five glacierised watersheds across the Himalayas to quantify the changes in seasonal and annual snow cover over the past 21 years and to analyse the meteorological factors influencing the SLA. Our findings revealed substantial variations in the SLA among sites in terms of seasonal patterns, decadal trends, and meteorological controls. SLA has been increasing in the Hidden Valley (+11.9 m yr^{-1}), Langtang Valley (+14.4 m yr^{-1}), and Rolwaling Valley (+8.2 m yr^{-1}) in the Nepalese Himalaya, but decreasing in the Satopanth (−15.6 m yr^{-1}) in the western Indian Himalaya, while we found no significant trend in Parlung Valley in southeast Tibet. We suggest that the increase in SLA was caused by warmer temperatures during the monsoon season in Nepal, whereas the decrease in SLA were driven by increased winter snowfall and reduced monsoon snowmelt in India. By integrating the outcomes of these analyses, we found that long-term changes in SLA are primarily driven by shifts in the local climate, whereas seasonal variability may be influenced by geographic features in conjunction with climate.

https://doi.org/10.5194/egusphere-2024-2026
Preprint. Discussion started: 7 August 2024

1 Introduction (as Heading 1)

Snow is an essential water resource in the high mountains of Asia (HMA), as it supplies melted water to downstream regions and regulates seasonal streamflow, especially during drought years (Pritchard, 2019; Kraaijenbrink et al., 2021). Mountain-sourced water supplies are increasingly sustaining human society through drinking, irrigation, industrial, and hydropower generation (Immerzeel et al., 2020; Viviroli et al., 2020). Snow has a cooling effect on the atmosphere by reflecting shortwave radiation and maintaining freezing ground temperatures, and decrease in the extent of snow has been suggested as one of the causes of high-elevation warming (Palazzi et al., 2019). Therefore, understanding the current and past snow cover distribution, its ongoing changes, and its driving factors are fundamentally important.

Several studies have addressed variations in snow cover in detail for individual watersheds (e.g., Gironoa-Mata et al., 2019; Stigter et al., 2017), whereas large-scale assessments have predominantly focused on annual values with moderate-resolution sensors (> 500 m) such as MODIS (Smith et al., 2018; Lievens et al., 2019; Tang et al., 2020; Kraaijenbrink et al., 2021). Analysis of seasonal variations in snow cover provides a more detailed information than annual values of snow dynamics and their relationships with climatic and geographic factors (Girona-Mata et al., 2019). While MODIS provides a daily temporal resolution and a broad perspective, the coarse spatial resolution of retrievals (500 m) poorly resolves topographic features, leading to the use of fractional snow cover products (Rittger et al, 2021). Because catchment-scale snow cover derived from MODIS can be affected by cloud cover owing to spectral similarities between clouds and snow (Stillinger et al, 2019), it can be biased by high-elevation snow-free areas and struggle with shadows and subpixel effects in the extreme high-relief topography of the Himalayas (Girona-Mata et al., 2019).

Snowline altitude (SLA) is a useful metric for studying snow cover variations on annual and seasonal timescales because it integrates both snowfall and snowmelt dynamics and is independent of catchment hypsometry (Girona-Mata et al., 2019; Deng et al., 2021). SLA is less biased by cloud cover than snow cover extent and is useful for evaluating hydrological models (Krajčí et al., 2014). On glaciers, SLA can also be used as a proxy for the equilibrium line altitude (Spiess et al, 2016; Racoviteanu et al., 2019). The seasonal pattern and aspect dependency of the SLA are particularly useful for revealing the primary controls on snow cover dynamics (e.g., Girona-Mata et al., 2019). Several previous studies have derived the SLA and its changes at various scales, such as individual catchments to continental scales (e.g., McFadden et al., 2011; Racoviteanu et al., 2019; Girona-Mata et al., 2019; Tange et al., 2020). However, none of these studies have examined SLA changes and the primary controls of SLA variations at a high resolution or in multiple regions to identify and understand regional differences.

Knowledge of the regional variation in the SLA and its sensitivity to climatic and geographic factors could provide an important basis for a deeper understanding of past and future changes in snow cover under climate change. Hence, this study aimed to answer the following research questions: 1. How does snowline seasonality vary across the climatic gradients of the Himalayas? 2. Do the controlling factors vary? 3. How much has the snowline shifted (in which months) over the past 20 years?

2 Study site and data

2.1 Study sites

We selected five glacierised catchments along the Himalayas (Fig. 1), where hydro-glaciological studies and glacier monitoring programs have been conducted in recent years. The catchments that we identified after the representative glacier, river, or valley were, from west to east, Satopanth, Hidden Valley, Langtang, Rolwaling, and Parlung (Fig. 1). The catchments have mean elevations ranging from 3,864 m to 5,384 m and include numerous glaciers covering 6.8% to 38.7% of the catchment area (Table

https://doi.org/10.5194/egusphere-2024-2026
Preprint. Discussion started: 7 August 2024

1). Although the Asian summer monsoon dominates the climate over its entire range, the monsoon intensity varies considerably across the five catchments. The Satopanth receives limited summer precipitation and moderate winter snow from westerly disturbances (Cannon et al., 2015; Bao et al., 2019), whereas the Parlung experiences considerable spring precipitation (Yang et al., 2013). In the other three regions, most annual precipitation occurred from June to September (Fig. S1).

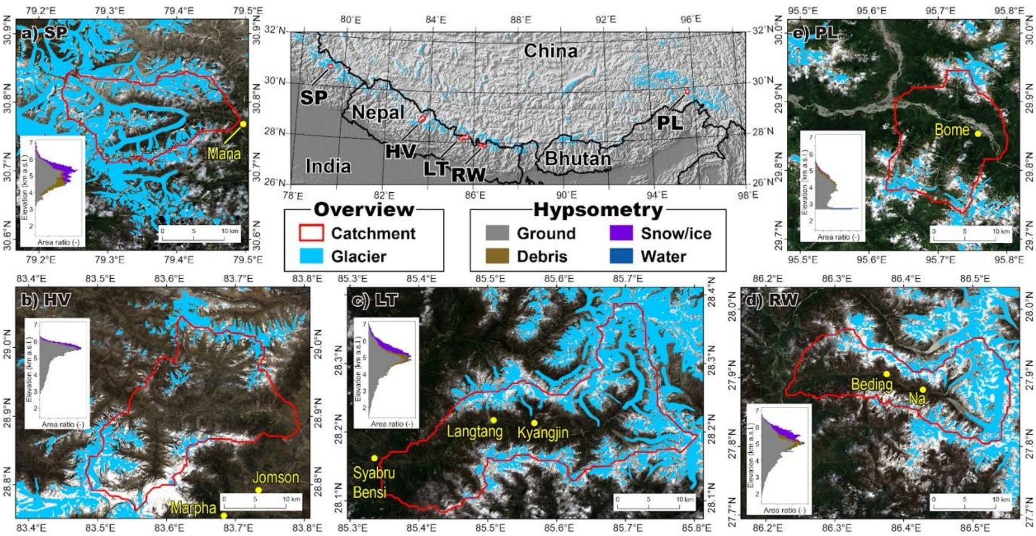

Figure 1: Upper center figure shows the location of target catchments (from west to east; Satopanth (SP), Hidden Valley (HV), Langtang (LT), Rolwaling (RW), Parlung (PL)). Enlarged views of target catchments are shown in surrounding figures; (a) Satopanth (SP), (b) Hidden Valley (HV), (c) Langtang (LT), (d) Rolwaling (RW), and (e) Parlung (PL). Catchment outlines and glaciers are indicated by red and light blue polygons, which are sourced from HydroSHEDS (Lehner and Grill, 2013) and GAMDAM (Sakai, 2019) databases, respectively. Yellow dots denote representative villages. The background images of (a)-(e) are composite images created using the Sentinel-2 images acquired between 2017 to 2020.

Table 2: Information on target catchments

	Central coordinate	Median altitude [m a.s.l.] (Max; Min)	Area [km^2]	Glacierised area [km^2]	Annual total precip. [mm]	Daily mean air temp. [℃]
Satopanth	79.36°E, 30.78°N	5,031 (7,080; 3,154)	243.0	94.0 (39 %)	1,654	− 7.5
Hidden Valley	83.63°E, 28.91°N	5,384 (6,492; 2,876)	445.0	49.1 (11 %)	801	− 8.4
Langtang	85.58°E, 28.21°N	4,879 (7,156; 1,461)	587.7	144.6 (25 %)	1,978	− 3.7
Rolwaling	86.41°E, 27.89°N	5,008 (6,897; 1,621)	309.5	76.8 (25 %)	1,170	− 3.9
Purlung	95.71°E, 29.84°N	3,864 (6,052; 2,678)	253.2	17.1 (7%)	2,056	− 2.2

https://doi.org/10.5194/egusphere-2024-2026
Preprint. Discussion started: 7 August 2024

2.2 Data

To determine the boundaries of the target catchments, we used HydroBASINS version 1.0 from the HydroSHEDS database (Lehner and Grill, 2013). HydroBASINS provides 12 levels of nested watershed boundaries according to their stream order, from which we chose level 9 for the target catchments, which is comparable in size to that used in Girona-Mata et al. (2019).

We used Level-1 top-of-atmosphere (TOA) reflectance for Landsat 5/7/8 data and Level-1C TOA reflectance for Sentinel-2 data to detect snow-covered areas (see Methods). The spatial resolutions of these datasets were 30 m for Landsat 5/7/8, 10 m for the visible bands of Sentinel-2, and 20 m for the SWIR bands of Sentinel-2. To select scenes, we identified all scenes from to 1999–2019 period whose internal metadata indicated a cloud cover of less than 50% of the scene. This resulted in 6,128 scenes: 1,384 for Satopanth, 1,173 for Hidden Valley, 967 for Langtang, 1,520 for Rolwaling, and 1,084 for Parlung.

Our method requires a reference digital surface elevation model (DEM); for this, we used the ALOS World 3D－30 m (AW3D30) version 2.2 which was produced from measurements by the Panchromatic Remote-sensing Instrument for Stereo Mapping (PRISM) on board the Advanced Land Observing Satellite (ALOS). The spatial resolution of AW3D30 is approximately 30 m (1-arcsecond mesh). The target accuracy of AW3D30 was set to 5 m (root mean square value) both vertically and horizontally (Takaku and Tadono, 2017).

We used three kinds of land surface classification data: (1) glacier outlines from the latest version of the GAMDAM inventory (Nuimura et al., 2015; Sakai, 2019), (2) outlines of supraglacial debris detected by Scherler et al. (2018), and (3) maps of surface water bodies named "Global Surface Water" created by the Joint Research Center (Pekel et al., 2016). These datasets were used to determine the catchment surface types and mask areas that may have been erroneously identified as snow, such as glaciers and water surfaces.

High-resolution multispectral images from RapidEye and PlanetScope were used to validate the SLA automatically detected using manual delineation. RapidEye and PlanetScope are both Earth observation constellations operated by Planet Labs, with spatial resolutions of 6.5 m and 3.7 m. We prepared one to three ortho-images for each target catchment that were obtained close to the date when automatic detections were conducted from the Landsat 5/7/8 or Sentinel-2 images. A list of the images used is shown in Table 2.

We obtained a 0.25° gridded near-surface 2 m air temperature, downward surface shortwave radiation, and precipitation from ERA5 (Hersbach et al., 2020). We aggregate the hourly products into daily and monthly mean datasets. The air temperature was corrected to the average snowline altitude during the target period (1999 –2019) in each catchment using a standard environmental lapse rate (0.065 ℃ m-1).

3 Method

3.1. Detection of snowline altitude

Our method to delineate snowline altitudes closely follows that of Girona-Mata et al. (2019) but is implemented in Google Earth Engine. A schematic diagram of the method is shown in Figure S2. In our detection tool, by inputting the latitude and longitude of a certain point, the catchment area containing the point was automatically selected from the HydroSHEDS database. Satellite images covering the catchment were collected from Landsat 5/7/8 and Sentinel-2 with a criterion of less than 50% cloud cover. In this study, an average of approximately 1,200 satellite images were collected for one catchment area over the past 21 years.

To determine the snow-covered area, we calculated the Normalized Difference Snow Index (NDSI) which is defined as the relative magnitude of the reflectance of the visible (green) and shortwave infrared (SWIR) bands. We used an NDSI threshold of

https://doi.org/10.5194/egusphere-2024-2026
Preprint. Discussion started: 7 August 2024

0.45 following Girona-Mata et al. (2019), which is relatively conservative but performs well against independent high-resolution measurements and spectral-unmixing approaches (Girona-Mata et al., 2019). Saturation issues are common in Landsat 5/7, where the input signal exceeds the maximum measurable signal and may bias the detected snow-covered areas; they have been improved in Landsat 8 and Sentinel-2. Rittger et al. (2021) evaluated the impact of band saturation using 25 images of Landsat 7 in the Himalayas and reported that 28% of snow-covered pixels were saturated in the visible bands. This problem was mitigated by selecting a conservative NDSI threshold (0.45) instead of a marginal threshold (0.4).

Next, we delineated the snowline from the derived snow cover map using the Canny edge detection algorithm (Canny, 1986) which produces smooth edges in images using a multistage process. However, at this point, the snowline may include misidentified areas because snow-covered areas are often obscured by clouds, shadows, scan line corrector (SLC) error stripes, or band saturation over snow. For example, the boundary of an obscured area may be misidentified as a snowline if clouds cover the actual boundary of a snow-covered area. Therefore, we removed snowlines from potentially erroneous areas such as cloud cover, deep shadows, SLC-error stripes (Landsat 7), and ice and water surfaces. The last two categories (removal of surface ice and water surfaces) were not implemented in Girona-Mata et al. (2019), but the NDSI can return high values for both surfaces, even when snow is not present (i.e., frozen water or bare glacier ice), which could bias the results. As per Girona-Mata et al. (2019), we also removed very small polygons (smaller than 35 pixels) to eliminate the effects of rock outcrops which may not be relevant to meteorological patterns (i.e., over steepened slopes that cannot hold snow).

Subsequently, the topographic aspect was calculated from the DEM to investigate orographic effects. This aspect was classified into four groups: east (45–135°), south (135–225°), west (225–315°), and north (315–360° and 0–45°). We then calculated the median snowline altitude for (i) the entire catchment, and (ii) each aspect group of each catchment. This process was repeated for all available images.

3.2. Manual delineation for evaluation of the automated approach

The automatically detected snowlines were compared with the manually delineated snowlines obtained using high-resolution ortho-images obtained near the date of automatic detection (within 10 days). In manual delineations, the location of the snowline was determined by checking high-resolution satellite images as well as the glacier outline and elevation data. Because it was difficult to distinguish snowlines on ridges, we created two sets of manually delineated snowlines: (i) snowlines extracted by excluding ridges or shadows (minimum extraction, orange lines in Fig. S3), and (ii) snowlines extracted without excluding ridges (maximum extraction; blue lines in Fig. S3). We then compared the median values and cumulative distribution of snowline altitude between the automatically detected and manually delineated snowlines.

To investigate the agreement of SLAs derived from different satellites, we compared the SLAs derived from Landsat 7, Landsat 8, and Sentinel-2 from 2016 to 2019. Landsat 5 data were excluded from this comparison because of the operational period (March 1984 to January 2013). This second check is important for determining whether snowlines derived using our method from sensors with different spatial and radiometric resolutions are biased relative to one another (Rittger et al, 2021).

3.3. Analysis of results

We first analysed the seasonality of the SLAs by considering a dual-phase harmonic regression (Eastman, et al, 2009) of the derived SLA values for the full period. The seasonal patterns of SLA in the first (1999–2009) and the second (2010–2019) half

https://doi.org/10.5194/egusphere-2024-2026
Preprint. Discussion started: 7 August 2024

decades are compared using T-tests (significant level = 0.05). For months with significant differences between the two periods, we examined the ERA5 climatic factors that could drive the SLA changes.

To examine long-term trends, satellite-derived SLA values for each scene were converted to a monthly mean. By linearly interpolating the missing values, the 21-year SLA trend was identified using the Mann-Kendall test (significance level = 0.01). We then examined the climatic factors driving SLA changes using multiple regression analysis for both annual variations (12-month moving averages) and longer-term changes (60-month moving averages).

The detected SLA was analysed to explore the effects of orographic and meteorological controls on seasonal and long-term variations. We investigated the disparities in SLA among aspect classes (east-, south-, west-, and north-facing slopes), interpreting the observed differences conceptually using the framework proposed by Girona-Mata et al. (2019). Additionally, we compare the 12-month and 60-month moving averages of the SLAs with those of climatic variables (air temperature, precipitation, and solar radiation) and assessed their statistical relationships through multiple regression analysis.

4 Results

4.1. Snowline evaluation

We first compared the detected SLAs from our method with those obtained through manual delineation of multiple scenes in each catchment to evaluate the reasonableness of the detected SLA. The SLAs obtained from our method exhibited a strong agreement with the manual delineation results for most scenes (Table 2), excellent agreement for three scenes (with a difference in SLA < 20 m), good agreement for six scenes (20 m < difference < 200 m), and fair agreement for two scenes (200 m < difference). The SLAs of the manual delineation used in the above comparison refer to the average of the two manual delineation results (maximum and minimum delineations; see Section 3.2). Subsequently, we compared the cumulative frequency of altitude at each grid point on the snowlines between the automatically and manually detected snowlines (Fig. S3). As depicted in Figure. S3, the three scenes demonstrating excellent agreement also exhibited remarkably consistent cumulative distributions, whereas the two scenes with fair agreement revealed a bias in the automatic detection results towards higher altitudes. The potential cause of the bias towards high altitudes is discussed in Section 5.3. For the remaining scenes (six scenes with good agreement), some variations in the cumulative frequency were observed; however, these differences were relatively minor and did not significantly affect the final SLA value, which represented the median of all detected altitudes on the snowlines in one scene. The scenes with fair agreement highlight that the method successfully identifies snow cover boundaries at high elevations that are often ignored by manual operators, resulting in a slightly higher statistical snowline altitude than that identified by manual operators.

Considering the intersatellite variability between the SLAs retrieved from Landsat 7, Landsat 8, and Sentinel-2 (Fig. S4), we observed the least variation in SLAs during the monsoon season (with a standard deviation σ of SLA for all sites and satellites < 18 m) and the largest variation during winter (σ < 140 m). Disagreements during winter were not unexpected given the inconsistent acquisition dates for the three satellites and the variable occurrence of winter snowfall in the Himalayas. Focusing on the differences in snowline altitudes (SLAs) between different satellites during the monsoon season, we observed a high degree of consistency in the range of SLA values within each catchment. Despite heavy cloud cover, the standard deviation in the median SLA between different satellites generally remained within 50 m, except for Parlung, where the deviation extended to 120 m. Although these variations may appear significant, they are relatively minor compared to the seasonal SLA variations observed for each sensor. Therefore, we consider the bias resulting from the use of different satellites in this study to be acceptable for examining seasonal and decadal changes in the SLA.

https://doi.org/10.5194/egusphere-2024-2026
Preprint. Discussion started: 7 August 2024

Table 2: Comparison of snowline altitudes (m a.s.l.) between the automatic detection and manual delineation. The SLA from manual delineation is the average value of two types of manual delineation results, with the maximum and minimum delineation results shown in square brackets after the average value. The data acquisition dates and used satellites are shown in brackets.

Catchment	SLA from automatic detection	SLA from manual delineation	Difference
Satopanth	5,330 (September 13, 2017, Landsat 8)	5,479 [5,445; 5,513] (September 13, 2017, RapidEye)	149
	4,634 (January 20, 2021, Landsat 8)	4,440 [4,726; 4,154] (January 27, 2021, PlanetScope)	194
Hidden Valley	5,530 (June 15, 2019, Sentinel-2)	5,536 [5,509; 5,564] (June 15, 2019, PlanetScope)	6
	5,387 (May 25, 2020, Sentinel-2)	5,406 [5,371; 5,441] (May 23, 2020, PlanetScope)	19
	5,675 (October 12, 2020, Sentinel-2)	5,498 [5,455; 5,540] (October 12, 2020, PlanetScope)	177
Langtang	4,615 (February 12, 2016, Landsat 8)	4,497 [4,457; 4,538] (February 13, 2016, RapidEye)	118
	4,665 (November 13, 2017, Landsat 8)	4,555 [4,443; 4,668] (November 12, 2017, RapidEye)	110
Rolwaling	5,213 (December 30, 2019, Landsat 8)	4,946 [5,067; 4,825] (December 30, 2019, PlanetScope)	267
	4,621 (April 20, 2020, Landsat 8)	4,285 [4,367; 4,202] (April 19, 2020, PlanetScope)	336
	4,892 (May 17, 2020, Sentinal-2)	4,881 [4,802; 4,961] (May 27, 2020, PlanetScope)	11
Parlung	3,841 (December 29, 2020, Landsat 8)	4,012 [4,012; 4,013] (December 29, 2020, PlanetScope)	171

4.2. Seasonality

Figure 2 shows the derived SLA values over the years, demonstrating strong seasonal variability despite considerable intraseasonal spread. Despite the relatively small number of images acquired during the monsoon period at all sites due to thick cloud cover, the derived SLAs for this period exhibit close agreement. Across most sites, two SLA peaks were observed during the monsoon and winter seasons, which is consistent with the findings of Girona-Mata et al. (2019). The double peak was more evident in Satopanth, Rolwaling, and Hidden Valley, which are located at high elevation but monsoon-dominated sites. A prominent peak during the monsoon was observed in Langtang Valley, whereas a moderate peak was noted in Parlung.

At all sites, the SLA reached its maximum during the monsoon season; however, the timing of the peak varied slightly among the sites: July in Langtang and August in Satopanth, Rolwaling, and Parlung. Hidden Valley showed a relatively stable SLA during the monsoon season, with a less pronounced maximum peak occurring in August (Fig. 2f). The minimum SLA occurred in late winter or early pre-monsoon at all sites: January in Langtang, February in Hidden Valley, March in Rolwaling and Parlung, and April in Satopanth. The SLA at Langtang began to increase in January, whereas the SLA at Satopanth continued to decrease until April. The particles exhibited a relatively flat winter SLA. The differences between the minimum and maximum SLAs varied from 480 m (Hidden Valley) to 1,100 m (Langtang).

https://doi.org/10.5194/egusphere-2024-2026
Preprint. Discussion started: 7 August 2024

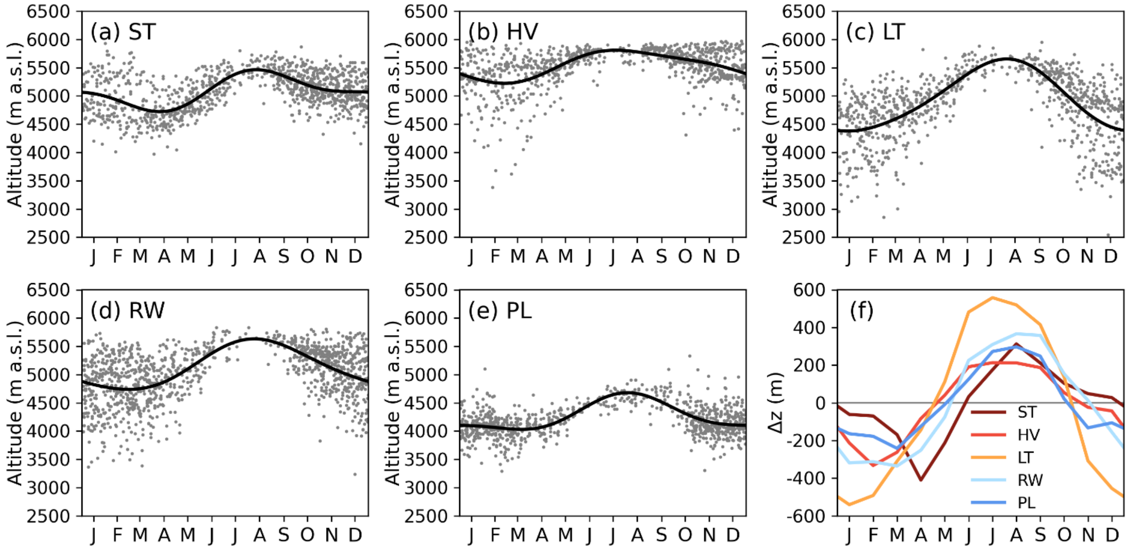

Figure 2: (a)-(e) The derived snow line altitude (SLA) over the target period (1999-2019) at each catchment and (f) the SLA anomaly from the mean SLA over the target period (1999-2019). Grey dots and solid lines in (a)-(e) show the SLAs derived from each satellite scene and smooth curves fitted with harmonic functions, respectively. Catchment abbreviations denote ST: Satopanth, HV: Hidden Valley, LT: Langtang, RW: Rolwaling, and PL: Parlung, respectively.

4.3. Trend in mean SLA

The time series of SLAs showed regionally different SLA trends (Fig. 3). Increasing SLA trends were found in Hidden Valley (+11.9 m yr^{-1}), Langtang (+14.4 m yr^{-1}), and Rolwaling (+8.2 m yr^{-1}), whereas Satopanth showed a decreasing trend (−15.6 m yr^{-1}) and Parlung showed no statistically significant trend (Fig. 3). These trends were confirmed for both 12-month and 60-month moving averages using the Mann-Kendall test, and the p-values for the four catchments where trends were detected were all less than 0.001. The elevational difference between the minimum and maximum SLAs, with 12-month moving averages for each catchment, varied between 580 m (Parlung) and 820 m (Langtang).

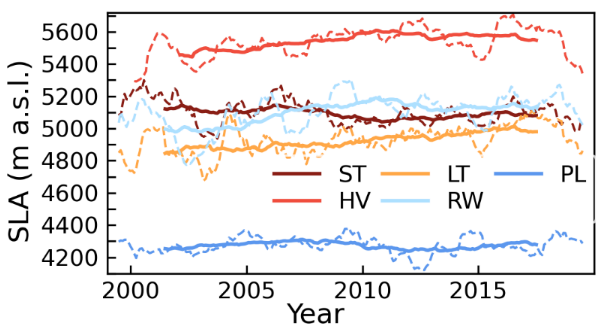

Figure 3: Snow line altitude with 60-month (solid lines) and 12-month (dashed lines) moving averages at the five target catchments. Trends are listed in Table 1. Catchment abbreviations denote ST: Satopanth, HV: Hidden Valley, LT: Langtang, RW: Rolwaling, and PL: Parlung, respectively.

https://doi.org/10.5194/egusphere-2024-2026
Preprint. Discussion started: 7 August 2024

4.4. Seasonal SLA aspect differences

Snowlines showed distinct seasonal patterns of SLA dependence (Fig. 4). A common characteristic among the five catchments was the minimal difference in SLA between aspects during the monsoon season, in contrast to the substantial SLA differences between aspects during winter. Additionally, the standard deviation in the SLA, represented by the error bars in Fig. 4, was smallest during the monsoon season, gradually increasing, and largest during winter. Regarding specific regional characteristics, Satopanth showed minimal differences in the SLA between aspects, even during winter, with only a slight decrease in the north-facing SLA. Conversely, aspect-induced differences were pronounced throughout the year in the Parlung region. Furthermore, Parlung exhibited a relatively small seasonal variability in the standard deviation of the SLA values.

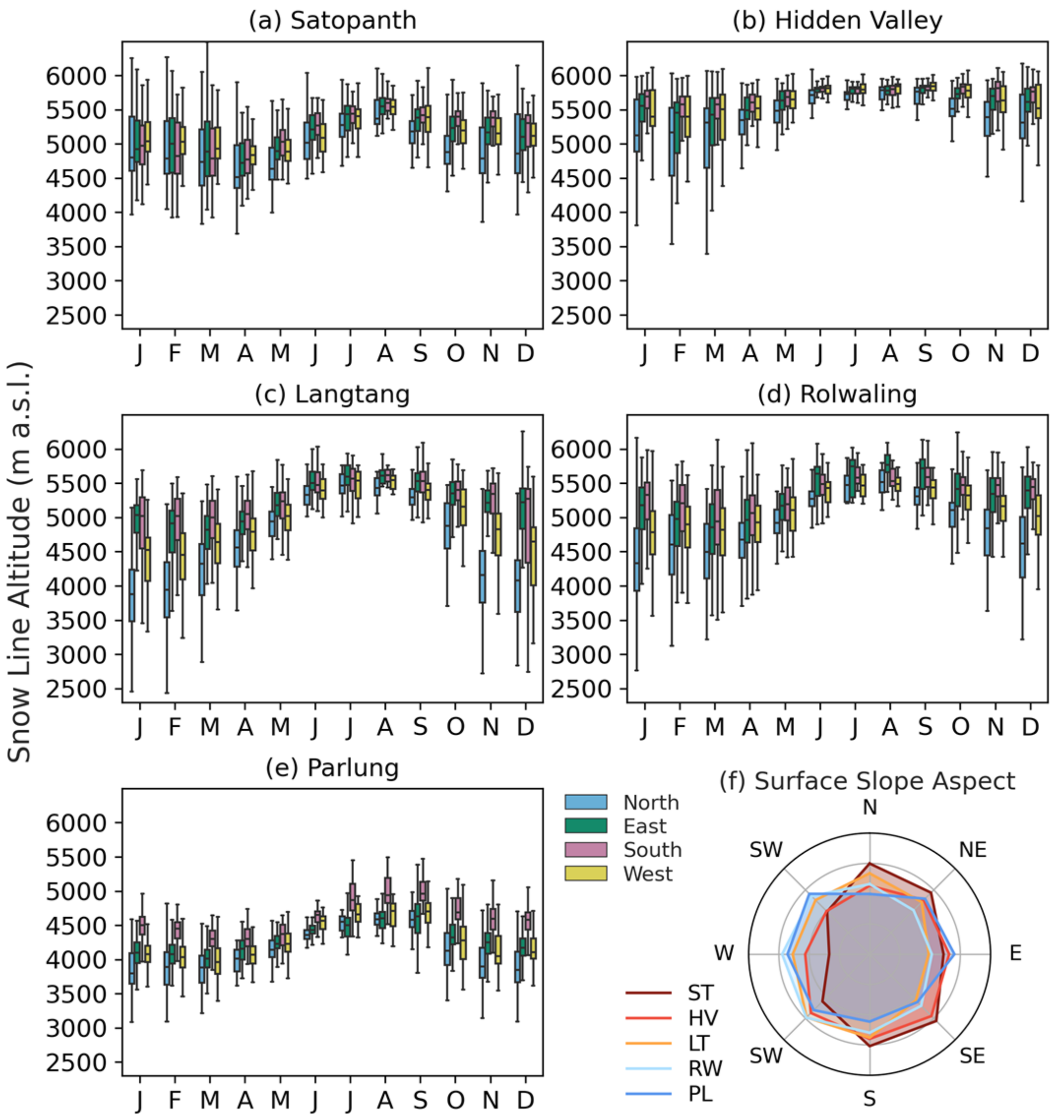

Figure 4: (a)-(e) Boxplots of monthly snow line altitude (SLA) for each aspect of the slope; north, east, south, and west. (f) Relative distribution of topographic aspects for each catchment (%).

https://doi.org/10.5194/egusphere-2024-2026
Preprint. Discussion started: 7 August 2024

4.5. Decadal changes in seasonal SLA

To examine the cause of the long-term changes in the SLA shown in Fig. 3, we compared the seasonal patterns of the SLA and climatic variables for the first half (1999-2009) and second half (2010-2019) of each catchment (Fig. 5). Focusing on the months with statistically significant changes, SLA decreases were found in March in Satopanth (Fig. 5a), Hidden Valley (Fig. 5b), and Rolwaling (Fig. 5d) and in January in Parlung (Fig. 5e). No significant seasonal SLA decrease was observed at Langtang (Fig. 5c). Increases in the SLA were evident in September in Satopanth (Fig. 5a), October to December in Hidden Valley (Fig. 5b), July and October in Langtang (Fig. 5c), and July, October, and November in Rolwaling (Fig. 5d). No significant increase was observed in Parlung (Fig. 5e). Overall, SLA decreases were primarily detected in winter to early spring, and increases in the monsoon and post-monsoon seasons.

The lowering of winter SLA could be attributed to the decrease in temperature in January across all regions where a decrease in winter SLA was detected. The increase in precipitation during February and March also contributed to the lowering of winter SLAs in Satopanth, Hidden Valley, and Rolwaling. No changes in solar radiation were observed, which could be related to a decrease in the winter SLA. On the other hand, the rising SLAs in the three Nepalese catchments (Hidden Valley, Langtang, and Rolwaling) were likely due to rising temperatures during the monsoon, which had a stronger effect on seasonal SLA than both precipitation increase and net shortwave decrease. Although the increase in precipitation during the monsoon season was also statistically significant in these three catchments, the SLA during the monsoon was controlled by the snow/rain transition altitude which was determined by the altitude dependence of air temperature (discussed in Section 5.1). Thus, it is plausible that the increase in temperature was the main factor contributing to the increase in SLA during the monsoon and post-monsoon periods. The decrease in solar radiation during the monsoon was statistically significant in the three Nepalese regions which is consistent with increased precipitation. It is unrealistic for the decrease in solar radiation to contribute to the increase in SLA, but it could suppress the increasing rate of the SLA. In contrast, the increasing solar radiation in November in Rolwaling may have contributed to the increase in the SLA in the same month. In Satopanth, an increase is observed only in September, suggesting an association with the temperature increase in the same month.

https://doi.org/10.5194/egusphere-2024-2026
Preprint. Discussion started: 7 August 2024

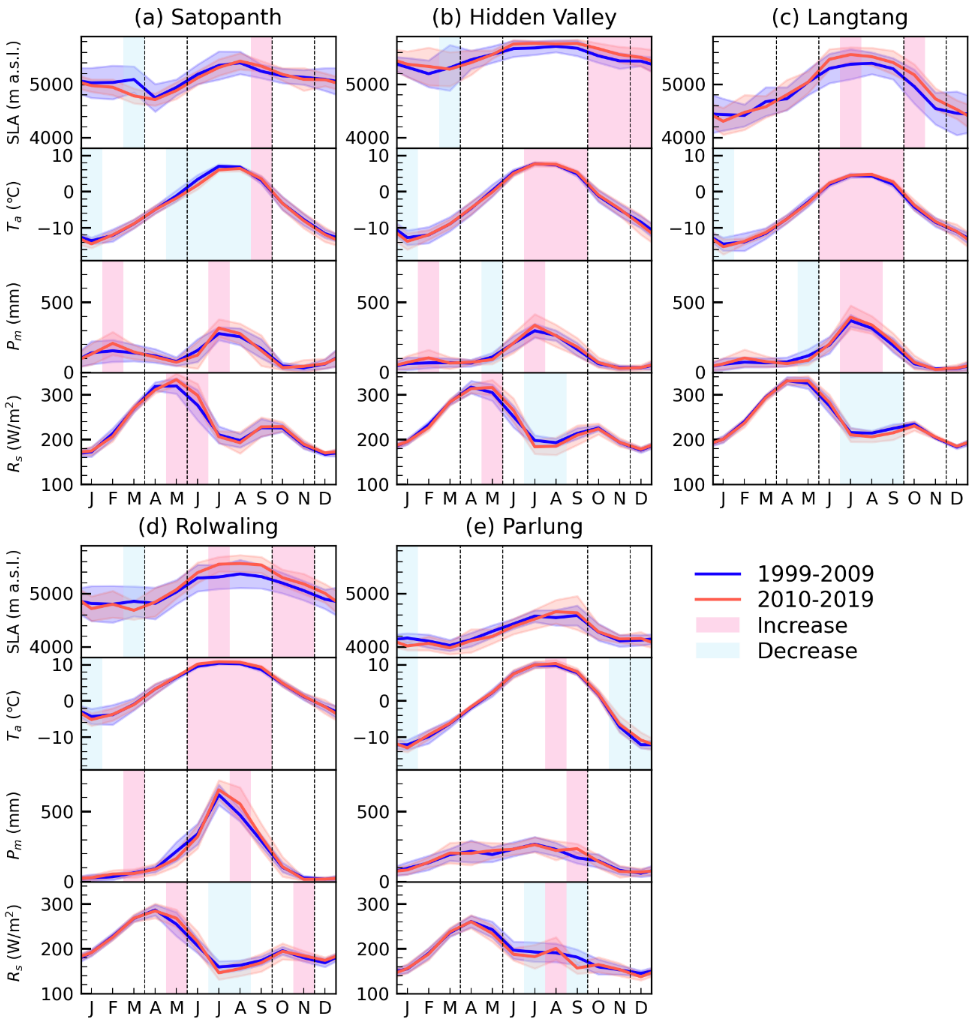

Figure 5: Monthly climatologies of SLA and climate variables (Ta: air temperature at 2-m height, Pm: monthly total precipitation, and Rs: daily mean downward solar radiation flux at the surface) for the first half (1999-2009 in blue) and the second half (2010-2019 in red), respectively. Shaded areas indicate statistically significant changes (pink for the increase and light blue for the decrease) between the periods.

4.6. Controlling factors for decadal trends in SLA

The 12-month moving averages of snowline altitude (SLA) exhibited significant correlations with changes in air temperature across most sites, except for Satopanth (Fig 6, Table 3). In Rolwaling, all three climatic variables demonstrated an influence on the SLA, with air temperature exhibiting the strongest impact, as evidenced by the largest t-value. Conversely, in Satopanth, precipitation emerged as the sole influencing factor, with a negative t-value, indicating that precipitation lowers the SLA. This finding that increased precipitation lowers the SLA is consistent with the results of Section 4.5 that increasing winter snowfall lowers the winter SLA at Satopanth. Overall, our results underscore the substantial influence of air temperature on SLA variation, which is consistent with previous research (Tang et al., 2020). This relationship is also expected to decisively control future snow climatology in the region (Kraaijenbrink et al., 2021). However, we also found that winter precipitation can serve as a significant driving factor,

https://doi.org/10.5194/egusphere-2024-2026
Preprint. Discussion started: 7 August 2024

particularly in Satopanth, where the SLA displays a decreasing trend. Although the influence of solar radiation is smaller than that of air temperature, it contributes to an increase in the SLA in Rolwaling.

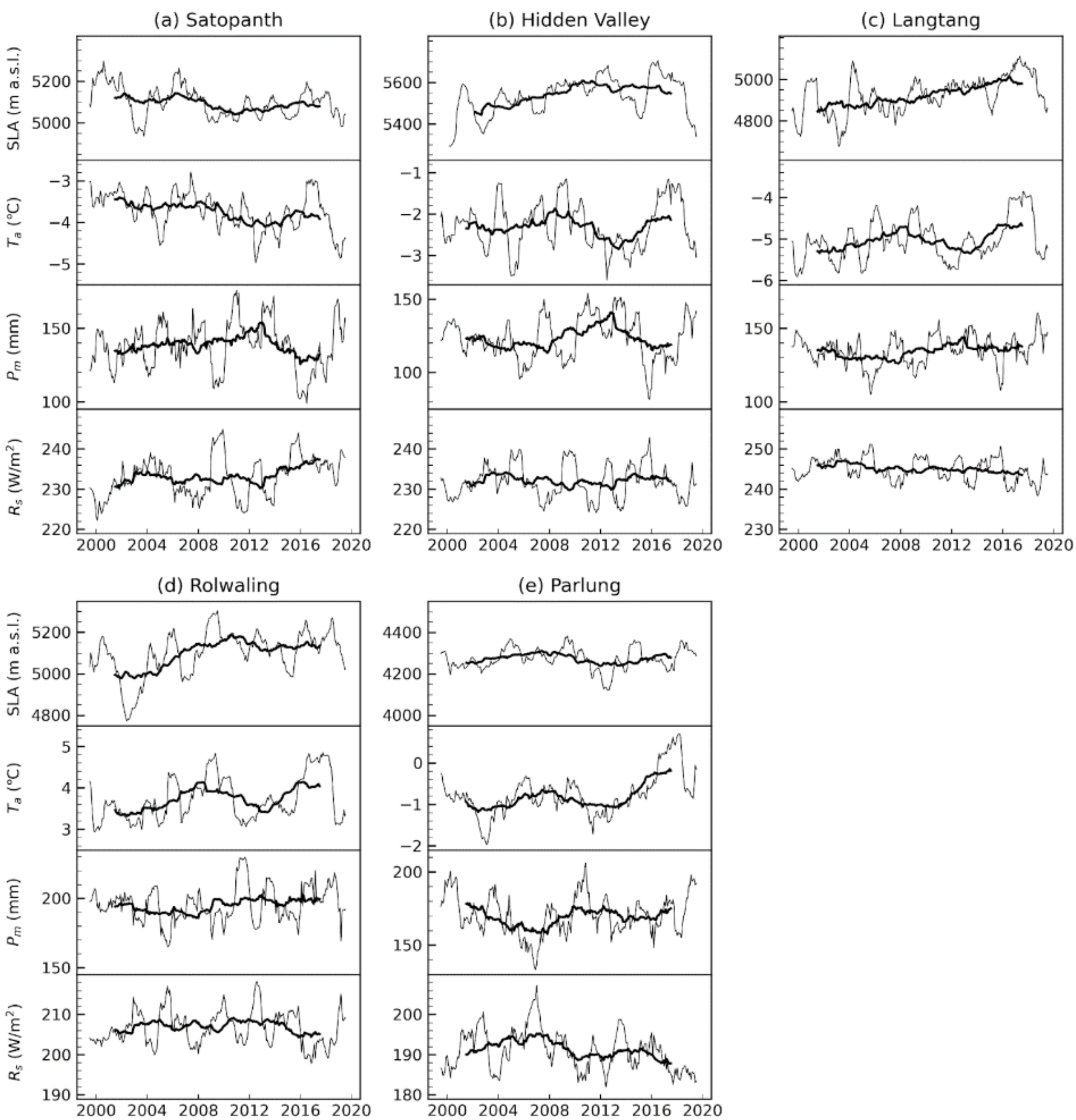

Figure 6: Time series of SLA and climate variables (Ta: air temperature at 2-m height, Pm: monthly total precipitation, and Rs: daily mean downward solar radiation flux at the surface) for the period from 1999 to 2019. Variables with 60-month and 12-month moving averages are drawn with thick and thin lines, respectively.

https://doi.org/10.5194/egusphere-2024-2026
Preprint. Discussion started: 7 August 2024

Table 3: Results of the multiple regression analysis using 12-month moving averages of climate data and SLA. Influential factors (p-value < 0.05 and |t-value| > 2.0) are shown in bold. A positive or negative t-value indicates a contribution to the increase or decrease of SLA, respectively.

		Coefficient	Standard error	t-value	p-value
Satopanth	Air temperature	6.14	11.07	0.56	0.579
	Precipitation	**−2.82**	**0.36**	**−7.89**	**<0.001**
	Solar radiation	−1.18	1.17	−1.01	0.108
Hidden Valley	Air temperature	**52.42**	**12.06**	**4.35**	**<0.001**
	Precipitation	−0.40	0.61	−0.65	0.516
	Solar radiation	1.54	2.14	0.72	0.472
Langtang	Air temperature	**95.14**	**11.28**	**8.44**	**<0.001**
	Precipitation	−0.33	0.77	−0.43	0.669
	Solar radiation	−2.84	2.81	−1.01	0.314
Rolwaling	Air temperature	**147.57**	**11.33**	**13.03**	**<0.001**
	Precipitation	**2.83**	**0.71**	**4.00**	**<0.001**
	Solar radiation	**9.95**	**2.20**	**4.52**	**<0.001**
Parlung	Air temperature	**30.37**	**8.41**	**3.65**	**<0.001**
	Precipitation	−0.29	0.24	−1.21	0.227
	Solar radiation	0.99	0.78	1.28	0.201

5 Discussion

5.1. Seasonal pattern & controls

We found consistencies and differences in the seasonal patterns across the five target catchments. Across the five regions, the SLA reaches its highest level during the monsoon summer and is maintained at a relatively stable snow/rain transition altitude caused by abundant precipitation and altitude dependence on air temperature (Girona-Mata et al., 2019). Once the precipitation reaches a sufficient level to maintain this altitude, additional precipitation has no further impact on the SLA. Solar radiation is less effective during the monsoon summer because of frequent and heavy cloud cover, leading to highly diffused shortwave radiation (Pellicciotti et al., 2011). However, Parlung was an exception, as indicated by the minimal differences in SLA between the aspects (Fig. 4). In Parlung, differences in SLA between aspects persisted even in summer (Fig. 4), suggesting that solar radiation still has an impact on SLA.

Snow is most abundant from late winter to early pre-monsoon, immediately before snowmelt begins. In Langtang, SLA showed the lowest peaks in January, indicating that snowmelt started in February as solar radiation increased. In contrast, Satopanth experienced a later peak with the lowest SLA in April. This region is less influenced by solar radiation throughout the year (Fig. 4); therefore, snowmelt may begin when temperatures increase.

https://doi.org/10.5194/egusphere-2024-2026
Preprint. Discussion started: 7 August 2024

Winter exhibits significant variability in the snowline altitude (SLA) across catchments, largely due to the influence of westerly storms. These storms sporadically cause heavy snowfall, leading to increased variability in the SLA. Particularly at Langtang and Rolwaling, the variability was pronounced, with more snow on the west-facing slopes than on the east-facing slopes, indicating the impact of westerly winds (Fig. 4). Conversely, Hidden Valley experiences less east-west variation and winter SLA variability than Langtang and Rolwaling. This could be attributed to the high-altitude Dhaulagiri mountain range to the southwest, which may act as a barrier to westerly winds, thereby limiting the inflow of moist air across the mountains. Despite being located further west, Satopanth exhibited minimal east-west variation in the SLA. The Satopanth Catchment features high-elevation ridges on its western side (Fig. 1).

Therefore, westerly winds may have deposited more snow on the outer western slopes of the catchment area. It is conceivable that winds crossing these western ridges contributed to snowfall within the catchment. This phenomenon may explain the reduced east-west disparity observed in Satopanth compared to regions directly impacted by prevailing winds. In contrast, Parlung, located on the southeastern Tibetan Plateau, is less influenced by westerly winds. Based on the above analysis, the seasonal patterns of SLA are not only dependent on climatic factors but are also significantly influenced by topography.

5.2. Trends, decadal changes in seasonality, and controls

Long-term trends and statistically significant explanatory variables exhibited similar patterns in the nearby regions (Fig. 3). Satopanth showed a declining trend, primarily driven by precipitation. In contrast, the three Nepalese regions exhibited increasing trends that were mainly influenced by temperature. Parlung showed no discernible trend, with fluctuations that were possibly related to temperature variations.

Based on the results presented in Section 4.5, we interpreted the monthly meteorological changes driving long-term variations in SLA. In Satopanth, the declining trend was primarily driven by a decrease in SLA in March. This decrease in SLA in March could be attributed to increased snowfall in February following a temperature decrease in January. This finding is consistent with that of a previous study that reported an increasing trend of synoptic-scale Western Disturbance activity over the past few decades, leading to increased winter precipitation in the western Himalayas (Krishnan et al., 2019). Conversely, the rising SLA in September may have moderated the decreasing rate of the interannual trend of SLA in Satopanth. In the three Nepalese regions, the increasing trends of SLA are driven by SLA increase during the monsoon to post-monsoon period, corresponding to rising temperatures during the monsoon season. Hidden Valley and Rolwaling also exhibited SLA lowering in March, possibly attributed to increased winter precipitation. In Parlung, a decrease in SLA due to lower temperatures was observed in January. However, this decrease in the January SLA was not sufficient to cause a long-term trend of declining SLA.

We anticipate that the long-term SLA trend is controlled by the balance between increased snowmelt during the monsoon and increased snowfall during winter. The balance between winter precipitation and summer temperature varied among the five catchments despite being located in the same Himalayan range. These results indicate that regions with different climatic and topographic characteristics, such as arid areas or those with winter accumulation, may have distinct factors controlling snow cover variability.

5.3. Limitations, advantages, and future perspectives

In our analysis, the largest discrepancy (7%) between the automated and manual extraction of snowline altitude (SLA) occurred in Rolwaling on April 19, 2020. The investigation revealed that the automated method incorrectly identified the boundaries between

https://doi.org/10.5194/egusphere-2024-2026
Preprint. Discussion started: 7 August 2024

the rocks and snow within high-elevation snowfields as snowlines. These protruding rock outcrops within snowfields differ from the snowline that manual operators would often identify; the lower boundary of the dominant snow cover. In our method, small polygons were removed to reduce the statistical relevance of these false positives; larger snow-free rock outcrops, however, are clearly prevalent in the Rolwaling domain. Even if such rock boundaries are not entirely removed, they generally have a small impact on the final SLA because they contribute relatively few grid points compared to the true snowline. In this particular scene, extensive cloud cover masked a large area, reducing the number of correctly identified snowline grid points (Fig. S5). In such cases, the influence of rock-snow boundaries is magnified, biasing the SLA towards higher elevations. The approach by Girona-Mata et al. (2019) involved masking elevations above a certain threshold to exclude ridgelines or rock outcrop snowlines. However, to achieve a globally applicable method, we did not apply a single definitive threshold. A potential solution is to exclude scenes in which the number of unmasked snowline grid points is too low, considering the possibility of significant error. Because of these errors, our automated extraction method may be unsuitable for pinpointing the exact snowline on a specific day, particularly under extensive cloud cover (introducing spatial bias based on the apparent snow boundaries). Nonetheless, it remains useful for analysing long-term trends and seasonal patterns over large areas.

An advantage of our method, compared to the standard snowline detection method leveraging MODIS data (Krajci et al., 2014), is its high sensitivity to snow at high altitudes, which comes from the high resolution of the satellites utilised. The coarse spatial resolution of MODIS snow cover products (500m) results in a crude representation of steeper topography, which leads to a high snow cover dropout rate at high elevations (e.g., Colleen et al., 2018), causing the detected SLA to easily jump to very high elevations in summer. Therefore, the SLAs obtained from MODIS were much higher than SLAs from our method at all sites during the monsoon season, as high-elevation snow was essentially undetected (Fig. S6). In contrast, the low-elevation discrepancies in SLAs appear to occur mainly in Satopanth and occasionally in Hidden Valley (Fig. S6). Upon examining the snowlines in Satopanth, we discovered that many north-facing slopes were shadowed by topography. As a result, our method, which masks shadows, tends to detect snowlines that are biased towards south-facing slopes. This likely explains the discrepancies observed at lower elevations in Satopanth, as snowlines detected on higher south-facing slopes were not fully captured. One option to address this issue is to apply a statistical correction, considering that we have measured the aspect difference and can identify which areas of the domain have been sampled versus those that have not. This correction would help provide a more accurate representation of the SLA across areas with various topographies.

Another advantage of the proposed methodology is its transferability. Although Landsat 5/7/8 and Sentinel-2 were selected for this study, additional satellite data could easily be included in the analysis if the data were stored in the Google Earth Engine. Using Landsat 9, launched in 2021, or other higher-resolution satellites that will be launched soon, will allow for longer and more detailed analyses. In addition, our method can be readily applied to a wider area because it automatically detects SLA using the Google Earth Engine.

Our study demonstrated significant regional differences in snow cover dynamics across the five catchments in the Himalayas, suggesting that various regions, such as arid areas or those where winter coincides with the rainy season, may have unique snow cover dynamics. By applying our automated method to broader areas, such as the whole of Asia or globally, we can investigate the distinct characteristics of snow dynamics in different regions. This approach will enable us to examine changes in the SLA worldwide and identify the factors controlling these changes, contributing to a deeper knowledge of the spatial and temporal distributions of snow cover and the hydrology in the cryosphere and downstream regions. Future works on SLA detection at larger scales could provide process-based advances beyond the foundations achieved with coarse sensors such as MODIS.

https://doi.org/10.5194/egusphere-2024-2026
Preprint. Discussion started: 7 August 2024

6 Conclusion

We propose an algorithm to automatically detect the snowline altitude (SLA) and apply it to five glaciated catchments in the High Mountain Asia (HAM) region. The SLA detected from 1999 to 2019 revealed regional consistencies and differences across the target catchments. The monthly time series of SLA indicated that the long-term trend of SLA varies from −15.6 m yr^{-1} to +14.4 m yr^{-1}: increasing in the three catchments in the Nepalese Himalaya, decreasing in Satopanth in the western Indian Himalaya, and showing no statistically significant changes in Parlung in southeastern Tibet. The analysis of decadal changes in the monthly SLA and climatic factors suggests that long-term SLA trends are primarily controlled by the balance between higher temperatures during the monsoon and lower temperatures with increased snowfall during winter. While time-series changes are strongly influenced by meteorological factors, seasonal patterns depend on topographical features, in addition to meteorological factors. Further application of our method on a broader scale could provide novel insights into the spatiotemporal variation in snow cover and its controlling factors. This will contribute to a deeper understanding of the future state of snow cover and related hydrology, which are crucial for water resource management and climate change adaptation.

Code availability

The script for automatic detection of SLA is available through the GitHub site.

Data availability

HydroSHEDS data, Landsat 5/7/8 data, and AW3D30 are available through the Earth Engine Data Catalog (https://developers.google.com/earth-engine/datasets/catalog/landsat) which is a data catalogue of the Google Earth Engine that is a cloud-based geospatial analysis platform. The latest version of the GAMDAM Inventory data used in this study are available on the PANGAEA website (https://doi.org/10.1594/PANGAEA.891423). Outline data for the supraglacial debris are available in the supplemental data of Scherler et al. (2018). Surface water body data are available from the official Global Surface Water website (https://global-surface-water.appspot.com/; Pekel et al., 2016). RapidEye and PlanetScope data are available from the European Space Agency (https://earth.esa.int/eogateway/missions/rapideye and https://earth.esa.int/eogateway/missions/planetscope). Finally, meteorological data from ERA5 were available via the Copernicus Climate Data Store (https://doi.org/10.24381/cds.adbb2d47; Hersbach et al., 2023).

Author contributions

ESM, FP, and KF designed the study. OS developed the automated algorithm and prepared the manuscript. OS analysed the data with the support of KF and AS. KF and AS manually delineated snowlines for validation. All authors discussed the analysis and results and contributed to the writing of the paper.

Competing interests

The authors declare that they have no conflict of interest.

Acknowledgments

We thank Maud Bernat for helping with the modification of the automatic detection code, and Michael McCarthy for preparing snowline data derived from the MODIS satellite.

Financial support

This research was supported by the JSPS-SNSF (Japan Society for the Promotion of Science and Swiss National Science Foundation) Bilateral Programmes project (HOPE, High-elevation precipitation in High Mountain Asia; JPJSJRP 20191503 / Grant 183633), and JSPS KAKENHI (Grant Number 23K13417 and 23H01509).

References

Bao, Y. and You, Q.: How do westerly jet streams regulate the winter snow depth over the Tibetan Plateau?, Clim. Dyn., 53, 353–370, https://doi.org/10.1007/s00382-018-4589-1, 2019.

Cannon, F., Carvalho, L.M.V., Jones, C., and Bookhagen, B.: Multi-annual variations in winter westerly disturbance activity affecting the Himalaya. Clim. Dyn., 44, 441–455, https://doi.org/10.1007/s00382-014-2248-8, 2015.

Mortimer, C. A. and Sharp, M.: Spatiotemporal variability of Canadian High Arctic glacier surface albedo from MODIS data, 2001–2016, The Cryosphere, 12, 701–720, https://doi.org/10.5194/tc-12-701-2018, 2018.

Deng, G., Tang, Z., Hu, G., Wang, J., Sang, G., and Li, J.: Spatiotemporal Dynamics of Snowline Altitude and Their Responses to Climate Change in the Tienshan Mountains, Central Asia, during 2001–2019, Sustainability, 13(7), 3992, https://doi.org/10.3390/su13073992, 2021.

Girona-Mata, M., Miles, E. S., Ragettli, S., and Pellicciotti, F.: High-resolution snowline delineation from Landsat imagery to infer snow cover controls in a Himalayan catchment, Water Resour. Res., 55, 6754–6772, https://doi.org/10.1029/2019WR024935, 2019.

Hersbach, H., Bell, B., Berrisford, P., Hirahara, S., Horányi, A., Muñoz-Sabater, J., Nicolas, J., Peubey, C., Radu, R., Schepers, D., Simmons, A., Soci, C., Abdalla, S., Abellan, X., Balsamo, G., Bechtold, P., Biavati, G., Bidlot, J., Bonavita, M., De Chiara, G., Dahlgren, P., Dee, D., Diamantakis, M., Dragani, R., Flemming, J., Forbes, R., Fuentes, M., Geer, A., Haimberger, L., Healy, S., Hogan, R. J., Hólm, E., Janisková, M., Keeley, S., Laloyaux, P., Lopez, P., Lupu, C., Radnoti, G., Rosnay, P., Rozum, I., Vamborg, F., Villaume, S., and Thépaut, J.: The ERA5 global reanalysis, Q J R Meteorol. Soc., 146, 1999–2049, https://doi.org/10.1002/qj.3803, 2020.

https://doi.org/10.5194/egusphere-2024-2026
Preprint. Discussion started: 7 August 2024

Immerzeel, W. W., Lutz, A. F., Andrade, M., Bahl, A., Biemans, H., Bolch, T., Hyde, S., Brumby, S., Davies, B. J., Elmore, A. C., Emmer, A., Feng, M., Fernández, A., Haritashya, U., Kargel, J. S., Koppes, M., Kraaijenbrink, P. D. A., Kulkarni, A. V., and Maye, J. E. M.: Importance and vulnerability of the world's water towers, Nature, 577, 364–369, https://doi.org/10.1038/s41586-019-1822-y, 2020.

Kraaijenbrink, P. D. A., Stigter, E. E., Yao, T., and Immerzeel, W. W.: Climate change decisive for Asia's snow meltwater supply, Nat. Clim. Chang, 11, 591–597, https://doi.org/10.1038/s41558-021-01074-x, 2021.

Krajčí, P., Holko, L., Perdigao, R. A. P., and Parajka, J.: Estimation of regional snowline elevation (RSLE) from MODIS images for seasonally snow covered mountain basins, J. Hydrol., 519(PB), 1769–1778, https://doi.org/10.1016/j.jhydrol.2014.08.064, 2014.

Krishnan, R., Sabin, T. P., Madhura, R. K. et al.: Non-monsoonal precipitation response over the Western Himalayas to climate change, Clim. Dyn., 52, 4091–4109, https://doi.org/10.1007/s00382-018-4357-2, 2019.

Lehner, B., and Grill, G.: Global river hydrography and network routing: baseline data and new approaches to study the world's large river systems. Hydrol. Process., 27, 2171-2186. https://doi.org/10.1002/hyp.9740, 2013.

Lievens, H., Demuzere, M., Marshall, H. P., Reichle, R. H., Brucker, L., Brangers, I., Rosnay, P., Dumont, M., Girotto, M., Immerzeel, W. W., Jonas, T., Kim, E. J., Koch, I., Marty, C., Saloranta, T., Schöber, J., and De Lannoy, G. J. M.: Snow depth variability in the Northern Hemisphere mountains observed from space, Nat. Commun., 10, 4629, https://doi.org/10.1038/s41467-019-12566-y, 2019.

McFadden, E. M., Ramage, J., and Rodbell, D. T.: Landsat TM and ETM+ derived snowline altitudes in the Cordillera Huayhuash and Cordillera Raura, Peru, 1986–2005, The Cryosphere, 5, 419–430, https://doi.org/10.5194/tc-5-419-2011, 2011.

Nuimura, T., Sakai, A., Taniguchi, K., Nagai, H., Lamsal, D., Tsutaki, S., Kozawa, A., Hoshina, Y., Takenaka, S., Omiya, S., Tsunematsu, K., Tshering, P., and Fujita, K.: The GAMDAM glacier inventory: a quality-controlled inventory of Asian glaciers, The Cryosphere, 9, 849–864, https://doi.org/10.5194/tc-9-849-2015, 2015.

Palazzi, E., Mortarini, L., Terzago, S., and Hardenberg, J.: Elevation-dependent warming in global climate model simulations at high spatial resolution, Clim. Dyn., 52, 2685–2702, https://doi.org/10.1007/s00382-018-4287-z, 2019.

Pekel, J. F., Cottam, A., Gorelick, N., and Belward, A. S.: High-resolution mapping of global surface water and its long-term changes, Nature, 540, 418–422, https://doi.org/10.1038/nature20584, 2016.

Pellicciotti, F., Raschle, T., Huerlimann, T., Carenzo, M., and Burlando, P.: Transmission of solar radiation through clouds on melting glaciers: a comparison of parameterizations and their impact on melt modelling, J. Glaciol., 57(202), 367-381, https://doi.org/10.3189/002214311796406013, 2011.

Pritchard, H.D.: Asia's shrinking glaciers protect large populations from drought stress, Nature, 569, 649–654, https://doi.org/10.1038/s41586-019-1240-1, 2019.

https://doi.org/10.5194/egusphere-2024-2026
Preprint. Discussion started: 7 August 2024

Racoviteanu, A. E., Rittger, K., and Armstrong, R.: An Automated Approach for Estimating Snowline Altitudes in the Karakoram and Eastern Himalaya From Remote Sensing, Front. Earth Sci., 7, 220, https://doi.org/10.3389/feart.2019.00220, 2019.

Rittgerm, K., Bormann, K. J., Bair, E. H., Dozier, J., and Painter, T. H.: Evaluation of VIIRS and MODIS Snow Cover Fraction in High-Mountain Asia Using Landsat 8 OLI, Front. Remote Sens., 2, 647154, https://doi.org/10.3389/frsen.2021.647154, 2021.

Sakai, A.: Brief communication: Updated GAMDAM glacier inventory over high-mountain Asia, The Cryosphere, 13, 2043–2049, https://doi.org/10.5194/tc-13-2043-2019, 2019.

Scherler, D., Wulf, H., and Gorelick, N.: Global assessment of supraglacial debris-cover extents, Geophys. Res. Lett., 45, 11798–11805, https://doi.org/10.1029/2018GL080158, 2018.

Smith, T. and Bookhagen, B.: Changes in seasonal snow water equivalent distribution in High Mountain Asia (1987 to 2009), Sci. Adv., 4, e1701550, https://doi.org/10.1126/sciadv.1701550, 2018.

Spiess, M., Huintjes, E., and Schneider, C.: Comparison of modelled- and remote sensing- derived daily snow line altitudes at Ulugh Muztagh, northern Tibetan Plateau, J. Mt. Sci., 13, 593–613, https://doi.org/10.1007/s11629-015-3818-x, 2016.

Stigter, E. E., Wanders, N., Saloranta, T. M., Shea, J. M., Bierkens, M. F. P., and Immerzeel, W. W.: Assimilation of snow cover and snow depth into a snow model to estimate snow water equivalent and snowmelt runoff in a Himalayan catchment, The Cryosphere, 11, 1647–1664, https://doi.org/10.5194/tc-11-1647-2017, 2017.

Stillinger, T., Roberts, D. A., Collar, N. M., and Dozier, J.: Cloud masking for Landsat 8 and MODIS Terra over snow-covered terrain: Error analysis and spectral similarity between snow and cloud, Water Resour. Res., 55, 6169–6184. https://doi.org/10.1029/2019WR024932, 2019.

Takaku, J., Tadono, T., Tsutsui, K., and Ichikawa, M.: Quality Improvements of 'AW3D' Global Dsm Derived from Alos Prism, IGARSS 2018 - 2018 IEEE International Geoscience and Remote Sensing Symposium, 1612-1615, https://doi.org.10.1109/IGARSS.2017.8128293, 2018.

Tang, Z., Wang, X., Deng, G., Wang, X., Jiang, Z., and Sang, G.: Spatiotemporal variation of snowline altitude at the end of melting season across High Mountain Asia, using MODIS snow cover product, Adv. Space Res., 66, 2629–2645, https://doi.org/10.1016/j.jhydrol.2022.128438, 2020.

Viviroli, D., Kummu, M., Meybeck, M., Kallio, M., and Wada, Y.: Increasing dependence of lowland populations on mountain water resources, Nat. Sustain., 3, 917–928, https://doi.org/10.1038/s41893-020-0559-9, 2020.

Yang, W., Yao, T. D., Guo, X. F., Zhu, M. L., Li, S. H., and Kattel, D. B.: Mass balance of a maritime glacier on the southeast Tibetan Plateau and its climatic sensitivity, J. Geophys. Res.-Atmos., 118, 9579–9594, https://doi.org/10.1002/jgrd.50760, 2013.